A Multidimensional Design for Dual Active Bridge Converters in Low-Voltage DC Systems

Hang Ren, *Student Member, IEEE*, Hanwen Zhang, *Graduate Student Member, IEEE*, Yanbo Wang, *Senior Member, IEEE*, Haoyuan Yu, *Member, IEEE*, Pingyang Sun, *Graduate Student Member, IEEE*, and Zhe Chen, *Fellow, IEEE*

***Abstract*—The dual-active-bridge (DAB) converter serves as a crucial galvanic isolating solution to provide dc grid-forming for dc elements in low-voltage direct-current (LVdc) systems. Key performance metrics such as efficiency, current stress, power density, and cost of DAB converter are chiefly subject to the optimal design of magnetic components and modulation strategies. However, existing DAB converter designs yield compromised solutions that optimize a limited subset of these metrics. This article develops a comprehensive analytical framework to characterize DAB converter operation across three key dimensions: 1) zero-voltage switching (ZVS) range; 2) power rating utilization; and 3) reactive power. To achieve a well-balanced design, a holistic optimization methodology is proposed, integrating multiobjective particle swarm optimization (MOPSO) with triple phase-shift control. By optimally selecting the transformer turns ratio and product of switching frequency and series inductance, the proposed MOPSO approach can collectively or selectively improve these performance aspects, enabling tailored DAB converter designs to meet diverse performance objectives. Experimental validation on a 1-kW DAB converter prototype demonstrates enhanced ZVS capability, improved utilization of converter rating, reduced reactive power, and achieves a peak efficiency over 95.9 %.**

***Index Terms*—Design optimization, dual-active-bridge (DAB) converter, phase-shift control, zero voltage switching (ZVS).**

Received 4 March 2025; revised 6 June 2025 and 4 August 2025; accepted 18 August 2025. Date of publication 20 October 2025; date of current version 23 January 2026. *(Corresponding author: Hanwen Zhang.)*

Hang Ren, Yanbo Wang, and Zhe Chen are with the Department of Energy, Aalborg University, 9220 Aalborg, Denmark (e-mail: hare@energy.aau.dk; ywa@energy.aau.dk; zch@energy.aau.dk).

Hanwen Zhang is with the Department of Electronic and Electrical Engineering, University of Bath, BA2 7AY Bath, U.K. (e-mail: hz2153@bath.ac.uk).

Haoyuan Yu is with the Department of Electrical Sustainable Energy, Delft University of Technology, 2600 AA Delft, The Netherlands (e-mail: h.yu-6@tudelft.nl).

Pingyang Sun is with the School of Electrical Engineering and Telecommunications, UNSW Sydney, Sydney, NSW 2052, Australia (e-mail: pingyang.sun@unsw.edu.au).

Digital Object Identifier 10.1109/TIE.2025.3603045

I. Introduction

LOW-VOLTAGE direct-current systems (LVdc) add critical capabilities to efficiently handle ever-growing volumes of distributed and renewable power. The dual active bridge (DAB) converter, as a widely used isolated dc/dc converter, is characterized by attractive features that include bidirectional power flow, wide voltage operating range, zero voltage switching (ZVS), and galvanic isolation [1]. In small-scale LVdc distribution networks, such as residential dc microgrids, nanogrids, and telecom or data center power trunks [2], [3], the DAB converter interfaces active front-end converters to the common dc bus, as shown in Fig. 1(a). In this configuration, each DAB converter regulates bus voltage and facilitates active power transfer to achieve dc grid-forming of interconnected elements [4]. By embedding a predefined voltage–power droop control, DAB converters operate locally within the allowable voltage ranges to share load and maintain bus voltage [5]. These applications drive the need for DAB converters design. Ensuring these converters performance across the full loads and wide voltage ranges is pivotal for improving the sustainability, resiliency, and long-term cost-effectiveness of LVdc systems.

The performance of a DAB converter is determined by three key dimensions: 1) ZVS range [6]; 2) power rating utilization [7]; and 3) internal reactive power [8], as given in Fig. 1(b). However, the relationships among these key dimensions are mutually coupled and against each other in check. For example, a smaller coefficient K_{fl}, defined as the product of series inductance L and switching frequency f_s, facilitates higher power transfer capability and lower reactive power by minimizing the required phase shift (PS) [8]. However, this comes at the compromise of reduced power rating utilization and higher capital costs. Therefore, optimized DAB converter performance is required through the parametrization of precisely engineered magnetic components and advanced phase-shift modulation strategies.

Optimal parameter design for DAB converter is driven by objective-specific considerations. Rodriguez et al. [9] examine the trade-off between expanding the ZVS range and minimizing reactive power. By adjusting the switching frequency and series inductance, it achieves either 100% ZVS or improved efficiency at full load. However, this single-objective optimization may not yield a well-balanced design that simultaneously accounts for

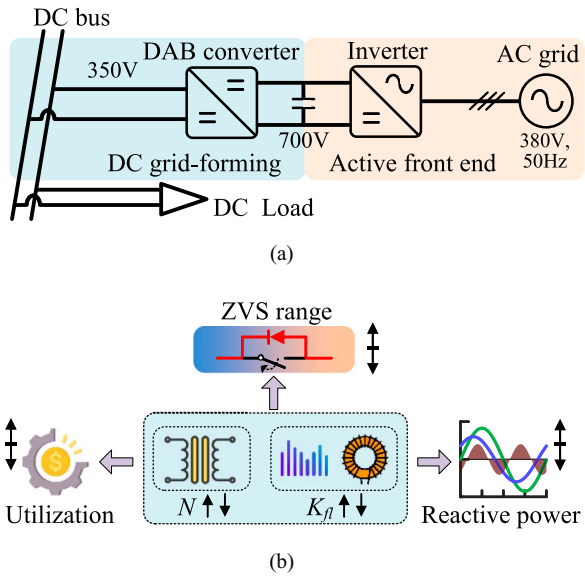

Fig. 1. (a) DAB converter serves as dc grid-forming in LVdc systems. (b) Relationship between design parameters and performance metrics.

power rating utilization and overall system cost. To overcome this limitation, Carvalho et al. [5] propose an effective unified coefficient that combines series inductance and switching frequency to optimize both the ZVS range and reactive power. This design limits the maximum PS angle to 13°, allowing room for further enhancement in power rating utilization of the DAB converter. Consequently, the power rating of active and passive components, including power switches, transformers, and capacitors, can be accordingly reduced to meet the reduced power rating, lowering overall capital costs. Recently proposed DAB converter optimization strategies are often tailored to specific applications. For instance, Das and Basu [10] employ triple phase-shift (TPS) modulation to minimize inductor rms current while maintaining full soft-switching. However, this method is tailored to high-ratio voltage conversion conditions [11]. Zhang et al. [12] optimally select magnetic components to minimize current stress under a wide output voltage range but assumes a fixed output current, limiting its general applicability. Therefore, developing a comprehensive analytical model that characterizes and optimizes all key DAB converter performance dimensions is essential for DAB converter design.

Advanced phase-shift modulation techniques, such as dual phase-shift, extended phase-shift, and TPS, can enhance the performance of DAB converters when the magnetic components are predetermined. For instance, Yang et al. [13] employ a Karush-Kuhn-Tucker algorithm-based TPS modulation, enabling ZVS for all power switches across the full load range. To add critical flexibility, Mou et al. [14] propose a five-degree-of-freedom modulation strategy to reduce current stress and expand the ZVS range. However, determining an optimal PS scheme requires calculations across nine modulation schemes, resulting in significant computational complexity. Artificial intelligence-based approaches, such as neural networks (NN) and deep reinforcement learning (DRL), provide promising solutions to reduce computational complexity. For example, Li et al. [15] use an NN with the PSO algorithm to establish a direct mapping between PS angles and inductor current, further minimizing current stress. Additionally, Tang et al. [16] applied DRL to select optimal TPS modes, reducing computational efforts and power switch losses. Despite these advancements, AI-driven modulation strategies do not fundamentally alter the original DAB converter design. These methods often overlook the critical impact of transformer turns ratio and inductance across the full load range. It is essential to have a holistic design approach that integrates both advanced modulation and optimized magnetic components to maximize power density and capacity utilization, ultimately leading to a more efficient and well-balanced DAB converter.

Specifically, unlike previous single-objective optimization studies that only considered individual performance such as ZVS range, power rating utilization, or reactive power separately, a comprehensive multidimensional design framework is proposed in this article. The main works are highlighted as follows.

1) A systematic multidimensional analytical framework is proposed, which simultaneously considers ZVS, power rating utilization, and reactive power to holistically enhance the DAB converter performance.
2) Formulation of a multiobjective optimization problem solved through the multiobjective particle swarm optimization (MOPSO) algorithm combined with TPS control strategy, jointly optimizing the transformer turns ratio and the product of series inductance and switching frequency.
3) Provision of a globally optimal, application-flexible design guideline adaptable to specific performance requirements, proven through comprehensive theoretical analysis and experimental validation.

II. DAB Converter Parametrization

A. DAB Converter Design Variables

In the design of DAB converter, the transformer turns ratio N, the switching frequency f_s, and the equivalent series inductance L are critical design variables that determine the DAB's voltage conversion gain, power capacity, and efficiency. As illustrated in Fig. 2(a), the DAB converter transfers power between two active bridges through a high-frequency transformer. The TPS modulation is employed in this work, as its three independent phase-shift variables provide enhanced flexibility in active and reactive power transfer and it achieves a wider ZVS region than SPS, DPS, and EPS. As shown in Fig. 2(b), D_1 and D_2 are the internal PS angles within primary and secondary bridges, respectively. D_3 is the outer PS angle between two active bridges.

The fundamental wave model is adopted in this article due to its compact expressions for active and reactive power, which directly reveal the impact of phase shift angles on converter performance, rather than the time domain model's piecewise linear

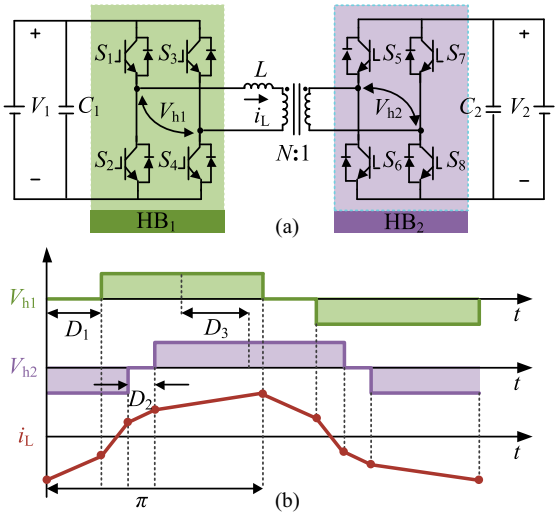

Fig. 2. (a) Topology of DAB converter. (b) Waveform of TPS control.

expression [8]. The active power transferred can be expressed by

$$P = \sum_{n=1,3,5,\ldots} \frac{4NV_1V_2}{n^3\pi^3 f_s L} \cos\left(n\frac{D_1}{2}\right) \cos\left(n\frac{D_2}{2}\right) \sin(nD_3) \tag{1}$$

where V_1 and V_2 are the dc terminal voltages, and n represents the order of fundamental and harmonic components. In the work, the first three odd harmonics ($n = 1, 3, 5$) are used to calculate for both active power and reactive power.

To simplify the analysis and improve design flexibility, switching frequency f_s and inductance L are combined into a single coefficient K_{fl}, which can be expressed in (2). Therefore, the design variables are simplified to transformer turns ratio N and coefficient K_{fl}. This reduction from a three-dimensional to a two-dimensional design space enhances computational efficiency. Once an optimal K_{fl} is determined, designers remain the flexibility to select specific f_s and L values that satisfy practical constraints such as switching losses, EMI requirements, or magnetic component sizing

$$K_{fl} = f_s \cdot L. \tag{2}$$

B. Conventional DAB Converter Design in LVdc Systems

In LVdc systems, the DAB converter supplies power P in proportion to the variation range of the dc bus voltage V_2, following droop curves set by codes and standards. As specified in [5], a DAB converter with a maximum power $P_{d\_max} = 5$ kW is designed to operate within an overvoltage of 540 V and an undervoltage of 250 V in a 350 V rated LVdc system, as shown in Fig. 3. Thus, the voltage ratio k of the DAB converter's input and output voltages is given by

$$k = \frac{V_1}{N \cdot V_2} = \frac{V_1}{N \cdot mV_{2b}}, \quad m \in [m_{\min}, m_{\max}] \tag{3}$$

where the input voltage $V_1 = 700$ V, $V_{2b} = 350$ V, m represents the normalized output voltage V_2. $m_{\min} = 250/350$ and

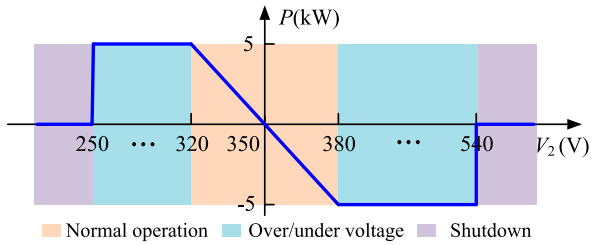

Fig. 3. Operation condition of DAB converter based on droop control.

$m_{\max} = 540/350$. In conventional DAB converter designs, the transformer turns ratio is chosen to match the input and output voltages for minimizing the current stress within the transformer [17]. Therefore, the conventional design set the transformer turns ratio as

$$N_c = \frac{V_1}{V_{2b}} = \frac{700}{350} = 2. \tag{4}$$

The coefficient K_{fl} is determined based on the DAB converter's maximum transmission power, ensuring sufficient power transfer at the minimum output voltage. Additionally, a 30% margin is typically incorporated to account for potential overload conditions. Therefore, the conventional K_{fl} is designed as given in

$$K_{fl\_c} = \frac{m_{\min} \cdot N \cdot V_1 \cdot V_{2b}}{8 \cdot 1.3 P_{d\_max}} = \frac{250 \times 2 \times 700 \times 350}{8 \times 350 \times 1.3 \times 5000} = 6.73. \tag{5}$$

III. Analysis on DAB Converters' Key Dimensions

A. ZVS Operation

The ZVS operation facilitates the improved efficiency of DAB converters. The ZVS condition is fulfilled by modulating the phase shift so that the inductor current reverses direction and commutes through the body diode of the switch before each switch TURN-ON, thereby discharging the device's junction capacitance and ensuring zero voltage across the switch at TURN-ON [18]. The ZVS range in this article is analyzed using PS modulation. Effects such as dead-time and parasitic junction capacitance, which affect the exact boundary conditions, are not considered in this work. Specifically, as shown in Fig. 4, when $t = t_1$, the inductor current i_L flows through the body diode of S_1, where it discharges the parallel capacitor of S_1 and charges the parallel capacitor of S_2. As a result, the voltage across S_1 drops to zero and S_1 turns on at zero voltage; simultaneously, S_4 achieves ZVS TURN-ON at $t = t_1$. When $t = t_3$, the inductor current i_L reverses to positive, enabling switches S_2 and S_3 to achieve ZVS TURN-ON.

With the TPS modulation control, the operation range of DAB converters is mapped into four modes by the boundary conditions P_1, $P_2(m)$ and $P_3(m)$. The derivation of TPS control and the boundary conditions can be found [12], [13]. Fig. 5 illustrates four efficient operation modes of DAB converter, including Mode $D_{m<1}$, Mode $D_{m>1}$, Mode F, and Mode G. The boundary conditions are given as

$$P_1 = \frac{V_1}{NV_{2b}} \tag{6}$$

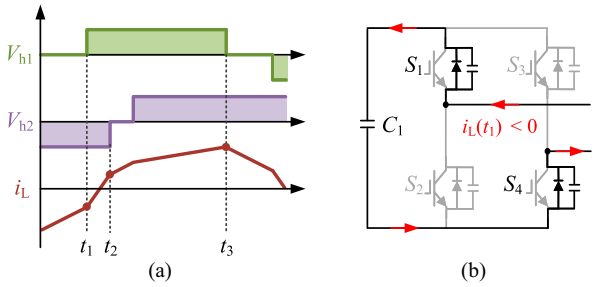

Fig. 4. Example of ZVS TURN-ON. (a) Voltage and current of HB1. (b) ZVS constraint.

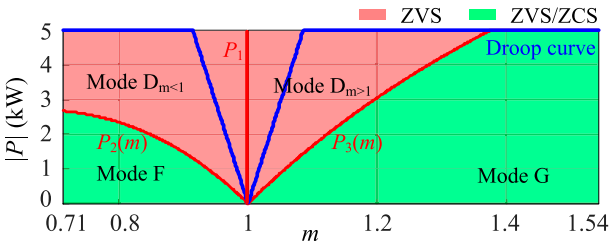

Fig. 5. ZVS region of DAB converter with TPS modulation.

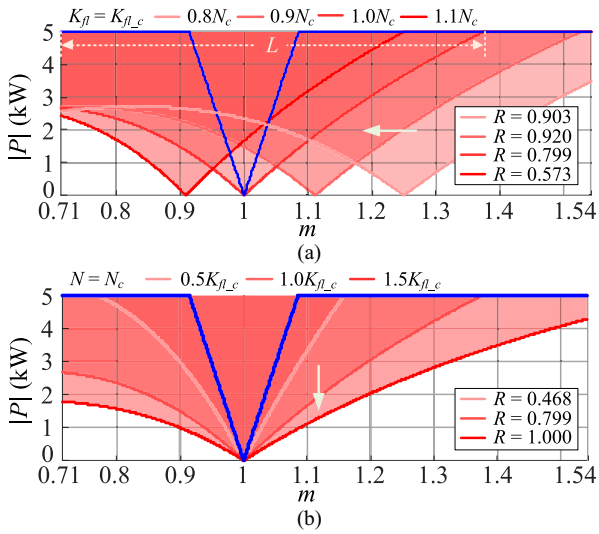

Fig. 6. (a) ZVS regions with different N when $K_{fl} = K_{fl\_c}$. (b) ZVS regions with different K_{fl} when $N = N_c$.

$$P_2(m) = \frac{N^2 V_{2b}^2 (V_1 m^2 - N V_{2b} m^3)}{4 V_1 K_{fl}} \tag{7}$$

$$P_3(m) = \frac{V_1^2 (N V_{2b} m - V_1)}{4 N V_{2b} K_{fl} m}. \tag{8}$$

The droop curve in Fig. 3 can be integrated into Fig. 5, which reveals that the curve falls within Mode D and Mode G. In Mode D, all switches can achieve ZVS, while Mode F and Mode G only support partial ZVS. However, the boundary conditions and ZVS range can be shifted by adjusting the design variables N and K_{fl}. Fig. 6 visualizes (6)–(8) to depict the variation in ZVS range with different sets of N and K_{fl}. Compared with the conventional design as shown in Fig. 6(a), when K_{fl} equals K_{fl_c}, increasing the turns ratio N shifts the ZVS region to the left, making it more reasonable for high voltage ratio applications. The proportion of the droop curve within Mode D, which quantifies the ZVS operation range of DAB converters is defined as R

$$R(N, K_{fl}) = \frac{L}{m_{\max} - m_{\min}} \tag{9}$$

where L in Fig. 6(a) represents the length of the droop curve within the ZVS region as $N = 1.0N_c$, while $(m_{\max} - m_{\min})$ denotes the total operation range. As N varies from $0.8N_c$ to $1.1N_c$, R initially increases and then decreases, indicating that the droop curve may not be fully covered. Fig. 6(b) depicts the role of K_{fl}, indicating that a higher K_{fl} facilitates a wide ZVS range when N remains constant. It is worth noting that $N = N_c$ serves as a critical requirement for achieving full ZVS operation by increasing K_{fl}. However, when $N \neq N_c$, full ZVS operation becomes unattainable, regardless of K_{fl}. Therefore, an optimal set of N and K_{fl} can maximize the ZVS operation range while ensures reasonable utilization and reactive power, which are analyzed in the following sections.

B. Power Rating Utilization

The power rating utilization η is defined as the ratio of the DAB converter's maximum expected active power output P_{d_max} in an LVdc system to its theoretical capacity $P_{\max}$. This theoretical capacity represents the maximum continuous power the DAB converter can deliver when operated at its full rating, as given in (10). η is determined by (11)

$$P_{\max} = \frac{m N V_1 V_{2b}}{8 K_{fl}} \tag{10}$$

$$\eta(N, K_{fl}) = \frac{P_{d\_max}}{P_{\max}} = \frac{8 P_{d\_max}}{V_1 V_{2\text{base}}} \cdot \frac{K_{fl}}{mN}. \tag{11}$$

Using conventional design parameters, the power rating utilization is calculated as $\eta = 76.92\%$ at $m = m_{\min}$. The LVdc system requires a maximum power transfer when the dc voltage reach the voltage limits. Therefore, evaluating power rating utilization at the minimum output voltage is critical to ensure sufficient power transfer capability of the DAB converter. Fig. 7 illustrates the relationship between η and both N and K_{fl} when the DAB converter operates over the maximum allowable voltage variation in the LVdc system. As observed, η is directly proportional to K_{fl} and inversely proportional to N. A 100% power rating utilization is achieved when $K_{fl} = 1.3K_{fl\_c}$ at $m = 0.71$, indicating that the DAB converter's maximum active power transfer capability precisely matches the LVdc system's power demand. This condition establishes $1.3K_{fl\_c}$ as the upper constrain for the DAB design; otherwise, the DAB may not be able to continuously supply the maximum load.

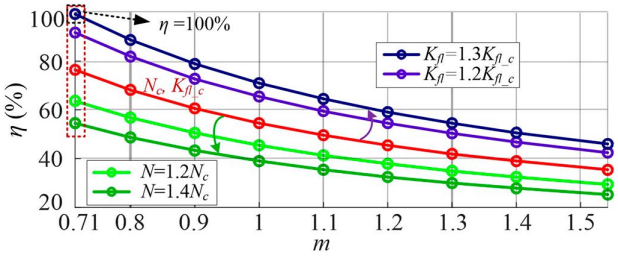

Fig. 7. Relationship between utilization η and N, K_{fl}.

C. Reactive Power Analysis

The DAB converter operates under the PS control, which inevitably induces a phase angle between the voltage and current in the transformer. As a result, reactive power circulates between the transformer's magnetic field and the converter's reactive components, which is represented as follows:

$$Q = \sum_{n=1,3,5,\ldots} \frac{4V_1 \cos\left(n\frac{D_1}{2}\right)}{n^3\pi^3 K_{fl}} \left[V_1 \cos\left(n\frac{D_1}{2}\right) - mNV_{2\text{base}} \cos\left(n\frac{D_2}{2}\right)\cos\left(nD_3\right)\right]. \quad (12)$$

To provide a comparative evaluation, reactive power is normalized by P_{d_max}, according to [8]. Fig. 8 shows the curves of normalized reactive power Q varied with m for different N and K_{fl} when the DAB converter operates under the droop control. As shown in Fig. 8(a), the curves of per unit (pu) reactive power Q shift downward as N increases, indicating an improvement in reducing reactive power. To further analyze the impact of N on reactive power across the entire operating range $(m_{\min}, m_{\max})$, the average reactive power Q_{avg} is represented as

$$Q_{\text{avg}} = \sum_{m=m_{\min}}^{m_{\max}} Q(m) / \left(P_{d\_max}\left(m_{\max} - m_{\min}\right)\right). \quad (13)$$

The results in Fig. 8(a) reveal that when $K_{fl} = K_{fl\_c}$, increasing N consistently reduces Q_{avg}, demonstrating that a higher transformer turns ratio minimizes reactive power. In contrast, as shown in Fig. 8(b), an increase in K_{fl} results in a higher Q_{avg} for $N = N_c$, suggesting that the adverse impact of a larger K_{fl} on reactive power. Therefore, Q_{avg} serves as a key metric for evaluating the combined impact of N and K_{fl} over the entire operating range.

The analysis reveals an inherent trade-off: increasing N reduces reactive power but lowers power rating utilization, while a higher K_{fl} expands the ZVS range and improves utilization but increases reactive power. This conflict between N and K_{fl} highlights the challenge of balancing key dimensions performance in DAB converter design.

IV. Proposed DAB Converter Design Method

A. Design Problem Formulation

The analysis in Section III reveals the design of transformer turns ratio N and inductance-switching frequency product K_{fl} in DAB converters, which can be formulated as an optimization

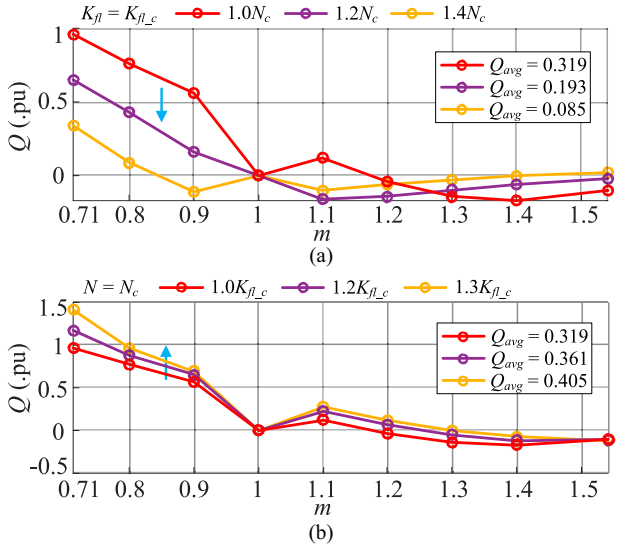

Fig. 8. Relationship between reactive power Q and N, K_{fl}. (a) Reactive power Q with different N when $K_{fl} = K_{fl\_c}$. (b) Reactive power Q with different K_{fl} when $N = N_c$.

problem. This approach ensures an optimal balance among three conflicting design objectives, expanding ZVS region, enhancing utilization, and minimizing reactive power. By optimizing design variables N and K_{fl} and adopting the TPS control, it can achieve the best possible trade-off among these competing objectives.

The optimization problem can be structured as follows:

$$\min_{N,K_{fl}} f(x) = [f_1(x), f_2(x), f_3(x)] = [(1 - R(x)), (1 - \eta(x)), Q_{\text{avg}}(x)] \quad (14)$$

subject to

$$\text{constraint 1: } P(N, K_{fl}) = \frac{m_{\min} N V_1 V_{2\text{base}}}{8K_{fl}} \geq P_{d\_max}$$
$$\text{constraint 2: } N \in \left[\frac{V_1}{m_{\max} V_{2b}}, \frac{V_1}{m_{\min} V_{2b}}\right] \quad (15)$$

where $f(x)$ is the objective function, $f_i(x)(i = 1, 2, 3)$ represents the objectives of maximizing ZVS region R and utilization η, and minimizing reactive power Q_{avg} respectively. x is $[N, K_{fl}]$ corresponding to the decision variables of optimization problem. Constraint 1 ensures that the DAB converter can achieve required power level at the minimum output voltage. Constraint 2 restricts the transformer turns ratio based on the criterion that the conversion voltage ratio remains close to unity [17].

B. Optimization Algorithm for Designing DAB Converters

The MOPSO algorithm is well-suited for problems with a relatively small number of decision variables and objectives, offering fast convergence and ease of implementation [19], [20]. Other algorithms, such as NSGA-II, are recognized for their robustness and strong ability to maintain diversity along the Pareto front, particularly in complex or high-dimensional

search spaces [21]. Considering these factors and the scale of our problem (two variables, three objectives), MOPSO algorithm is selected for its computational efficiency and reliable convergence.

As formulated in (14), the optimization problem involves two decision variables, transformer turns ratio N and inductance-switching frequency product K_{fl}, defining a two-dimensional particle position space. The algorithm begins by initializing a swarm of particles, where each particle represents a candidate solution with specific values of N and K_{fl}. Through iterative position updates based on predefined update rules, the particles navigate the solution space, progressively converging toward optimal solutions that maximize the ZVS region and utilization while minimizing reactive power.

The velocity of each particle is updated based on its historical best position P_{best} and the global best position G_{best} of the swarm. It can be expressed as

$$v_i^{k+1} = \omega v_i^k + c_1 r_1 (P_{\text{best}}^k - X_i^k) + c_2 r_2 (G_{\text{best}}^k - X_i^k) \quad (16)$$

where k is iteration number, v_i^k, X_i^k is current velocity and position of particle i, ω is inertia weight, c_1 and c_2 are acceleration constants. The new position of each particle is updated as

$$X_i^{k+1} = X_i^k + v_i^k. \quad (17)$$

The process of MOPSO algorithm for searching the optimal solutions N and K_{fl} is outlined as follows.

1) *Initialization:* The MOPSO parameters are initialized, and random values for the decision variables N,K_{fl} are generated within the constraint (15).
2) *Fitness Evaluation:* Each particle's fitness is evaluated based on the objective functions (14), and both personal best P_{best}^k and global best G_{best}^k positions are updated.
3) *Velocity and Position Update:* Particle velocities v_i^{k+1} and positions X_i^{k+1} are updated using the best-known positions, driving particles iteratively toward the optimal solutions.
4) *Termination and Solution Storage:* The algorithm continues until the maximum iteration limit is reached, at which point the Pareto-optimal solutions for N and K_{fl} are stored.

To prevent premature convergence and ensure sufficient exploration of the Pareto front, several strategies were incorporated in the MOPSO algorithm. An adaptive grid-based archive management was used to maintain diversity, with solutions in less-crowded grids [22]. The archive size was limited to 200 nondominated solutions, and a self-adaptive mutation mechanism was introduced when repeated constraint violations occurred [23]. In addition, the inertia weight was linearly decreased from 0.8 to 0.2 to balance global search and local exploitation throughout the optimization process. The detailed MOPSO hyperparameters are shown in Table I.

TABLE I
HYPERPARAMETERS FOR MOPSO ALGORITHM

Hyperparameter	Value
Population size	100
Maximum number of iterations	600
Inertia weight	0.8
End weight	0.2
Acceleration coefficients	$c_1 = c_2 = 1.495$

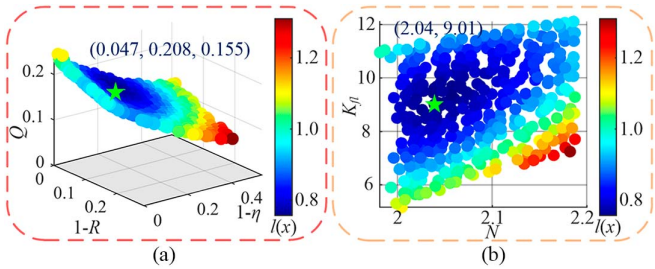

Fig. 9. Optimization results for case 1. (a) Optimization objectives R, η and Q_{avg}. (b) Design variables N and K_{fl}.

C. Proposed DAB Converters Design Guidelines

This article provides a holistic framework for optimizing DAB converter design by adjusting the objective function in (14) to meet global or specific performance requirements. Table II classifies the design objectives, trade-offs, and decision variables into four categories. It should be noted that in the purpose of comparing with existing design methods, the operating range m is set between $m = 0.914$ (320 V/ 350 V) and $m = 1.09$ (380 V / 350 V), and power transmission follows the droop control curve in Fig. 3.

1) Case 1 - Global Optimization of R, η, and Q_{avg}: To achieve a well-balanced DAB converter design, the design problem is formulated in (14) with constraints defined in (15). By applying the MOPSO algorithm, the optimization process will efficiently explore the design space and identify the Pareto-optimal solutions for N and K_{fl}, ensuring an optimal trade-off among the three objectives.

Fig. 9 shows the optimized solutions of the proposed MOPSO algorithm for DAB converter design. Fig. 9(a) shows all possible sets of R, η and Q_{avg}. This three-dimensional plot illustrates the trilemma among the three objectives. To better understand Fig. 9(a), the color gradient $l(x)$ indicates the Euclidean distance of each solution from the origin, where the lower values of $l(x)$, closer to the point of (0, 0, 0), correspond to solutions with a better balance among objectives. The $l(x)$ is expressed as

$$l(x) = \sqrt{\sum_{i=1}^{n} \omega_i \left(\frac{f_i(x) - f_i^{\text{best}}}{f_i^{\text{worst}} - f_i^{\text{best}}} \right)} \quad (18)$$

where n is the number of objective functions. f_i^{best} represents the ideal point corresponding to design objectives that is (0, 0, 0). f_i^{worst} is the farthest point from the ideal point. ω_i is the weight for each objective, and it is defined by designer to reflect different performance priorities. In this article, all weights are set equally ($\omega_i = 1$) to demonstrate global optimization. The green star marks the optimal solution at $R = 95.3\,\%$,

TABLE II
DAB CONVERTER DESIGN CLASSIFICATION BASED ON DIFFERENT OBJECTIVES

Category	Design Objectives			Trade Off	Problem Formulation	Design Variables	Constrains
	ZVS Region(R)	Utilization(η)	Reactive Power(Q_{avg})				
Case 1	●	●	●		(14)	N, K_{fl}	(15)
Case 2	$R = 100\ \%$	●	●		(23)	K_{fl}	(15), (21)
Case 3	●	$\eta = 76.92\ \%$	●		(25)	N, K_{fl}	(24)
Case 4	\	\	●	Single objective optimization	(26)	N, K_{fl}	(15)

$\eta = 79.2\,\%$, $Q_{\text{avg}} = 0.155$ pu with the smallest $l(x)$, indicating the best trade-off.

Fig. 9(b) shows the corresponding values of N and K_{fl} for each solution, with the optimal point at (2.04, 9.01). This set of Pareto-optimal solutions provides a precise configuration of N and K_{fl} that optimally balances the R, η and Q_{avg}, leading to global optimization performance in DAB converters.

2) Case 2 - Optimization of η and Q_{avg} With R Fixed at 100%: To minimize switching losses and enhance DAB converter efficiency, achieving full ZVS operation is crucial. As the previous analysis in Fig. 6(a), full ZVS requires a conversion voltage ratio of $k = 1$, from which the transformer turns ratio can be derived as follows:

$$N = \frac{V_1}{V_{2b}} = 2. \tag{19}$$

It is important to ensure that the droop curve remains fully enclosed within the ZVS region to achieve the 100 % range by adjusting K_{fl}, as shown in Fig. 5. Therefore, the boundary conditions must lower than the droop curve

$$\max(P_2(m_{\min}), P_3(m_{\max})) \le P_{d\_max}. \tag{20}$$

By substituting the expression of $P_2(m_{\min})$ and $P_3(m_{\max})$ (7) and (8) into (20), the range of K_{fl} can be given in

$$\max\left(\frac{N^2V_{2b}^2(V_1m_{\min}^2 - NV_{2b}m_{\min}^3)}{4V_1P_{d\_max}}, \frac{V_1^2(NV_{2b}m_{\max} - V_1)}{4NV_{2b}m_{\max}P_{d\_max}}\right) \le K_{fl}. \tag{21}$$

Taking parameters into constraints (15) and (21), the range of design variable K_{fl} can be derived as

$$1.9342 \le K_{fl} \le 8.6975. \tag{22}$$

The above assumptions ensure a 100 % ZVS. Therefore, the optimization problem is formulated as (23). Then, the MOPSO algorithm is employed to identify the optimal value K_{fl}

$$\min_{K_{fl}} f(K_{fl}) = [f_2(K_{fl}), f_3(K_{fl})] = [(1 - \eta(K_{fl})), Q_{\text{avg}}(K_{fl})]. \tag{23}$$

Fig. 10 shows optimization results for K_{fl}. It can be seen that the trade-off between objectives utilization and reactive power is visualized in a two-dimensional plot, where the optimal solution is found with $\eta = 69.1\,\%$ and $Q_{\text{avg}} = 0.147$ pu. Meanwhile, the optimal solution for K_{fl} is found at 7.7, as shown in Fig. 10(b).

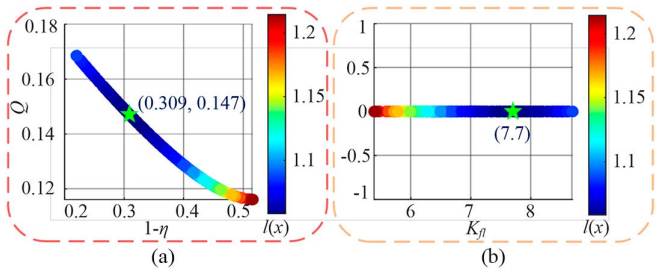

Fig. 10. Optimization results for case 2. (a) Optimization objectives η and Q_{avg}. (b) Design variables K_{fl}.

3) Case 3 - Optimization of R and Q_{avg} With η Fixed at 76.92 %: Taking into account an overload margin of 30 % of the DAB converter, η is set to 76.92 % according to (11). However, operators can customize η based on specific requirements, such as volume, economics, and power density. The constraint can be derived through the utilization equation

$$\eta = 76.92\% = \frac{8P_{d\_max}}{V_1V_{2\text{base}}} \cdot \frac{K_{fl}}{m_{\min}N} \tag{24}$$

where the transformer turns ratio N and inductance-switching frequency product K_{fl} are selected as design variables. The ZVS region R and reactive power Q_{avg} are selected as design objectives. The optimization problem is structured as

$$\min_{N,K_{fl}} f(x) = [f_1(x), f_3(x)] = [(1 - R(x)), Q(x)]. \tag{25}$$

Fig. 11(a) presents the optimization results for R and Q_{avg} with $\eta = 76.92\,\%$. The Pareto-optimal solutions form a trade-off curve, with the optimal point at $R = 94.5\,\%$ and $Q_{\text{avg}} = 0.151$ pu. Fig. 11(b) exhibits the corresponding design variables, where the optimal values are $N = 2.04$ and $K_{fl} = 8.74$.

4) Case 4 - Single objective optimization Q_{avg}: To reduce reactive power, a single-objective optimization is applied to minimize Q_{avg}, which is formulated as (26)

$$\min_{N,K_{fl}} f(x) = Q(x). \tag{26}$$

This optimization should follow the two constraints in (15), and the PSO algorithm is utilized to select the optimal values for N and K_{fl}.

Fig. 12 presents the optimization results. It can be seen that Q_{avg} reduces as $l(x)$ is approaching the point (0, 0), reaching an optimal value of $Q_{\text{avg}} = 0.096$ pu. The corresponding

TABLE III
COMPARISON RESULTS OF DIFFERENT DESIGN METHODS

Optimization Objectives	Design Method	Design Variables	Modulation	ZVS Region R	Utilization η	Reactive Power Q_{avg}	$l(x)$
Increasing the ZVS region R	Ref. [9]	$N=2,\ K_{fl}=10.19$	SPS	100 %	91.4 %	0.207 pu	1.239
	Proposed (case2)	$N=2,\ K_{fl}=7.70$	TPS	100 %	69.1 %	0.147 pu	1.058
Optimization of R and Q_{avg} with $\eta=76.92\,\%$	Conventional	$N=2,\ K_{fl}=8.62$	TPS	100 %	76.92 %	0.167 pu	1.008
	Proposed (case3)	$N=2.04,\ K_{fl}=8.74$	TPS	94.5 %	76.92 %	0.151 pu	0.935
Minimize current stress and reactive power Q_{avg}	Ref. [5]	$N=2,\ K_{fl}=3$	SPS	100 %	26.9 %	0.204 pu	0.921
	Ref. [12]	$N=1.96,\ K_{fl}=6.26$	TPS	92.3 %	57.3 %	0.157 pu	0.709
	Proposed (case4)	$N=2.18,\ K_{fl}=7.28$	TPS	71.4 %	59.9 %	0.096 pu	0.433
Optimization R,η,Q_{avg}	Proposed (case1)	$N=2.04,\ K_{fl}=9.01$	TPS	95.3 %	79.2 %	0.155 pu	0.753

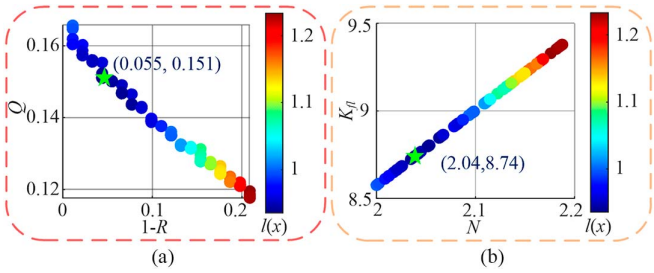

Fig. 11. Optimization results for case 3. (a) Optimization objectives R and Q_{avg}. (b) Design variables N and K_{fl}.

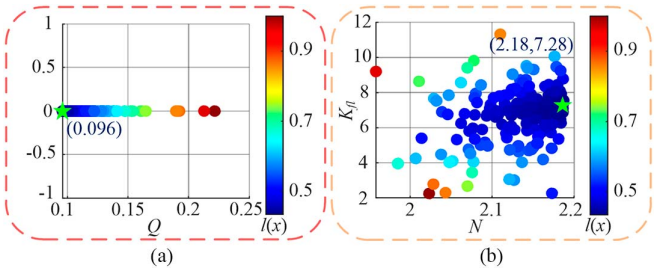

Fig. 12. Optimization results for case 4. (a) Optimization objectives Q_{avg}. (b) Design variables N and K_{fl}.

design variables are identified as $N = 2.18$ and $K_{fl} = 7.28$. The clustering of the solutions demonstrates the effectiveness of the PSO algorithm in attaining a precise configuration that minimizes Q_{avg}.

The proposed design framework includes ZVS capability, power rating utilization, and reactive power as primary objectives. The optimized transformer turns ratio N and series inductance L values thus obtained serve as fundamental guidelines. Once these parameters are determined, the DAB converter can be further fabricated at the component level, such as transformer winding design, component selection, PCB layout, IC-driver choice, realizing an optimal prototype. Therefore, the proposed methodology is applicable to both low-power and high-power applications by incorporating additional considerations.

D. Comparison With Existing Methods

Table III compares the proposed design method with existing approaches across different optimization objectives.

To ensure 100 % ZVS region, Rodriguez et al. [9] designed the series inductance and limits the maximum PS angle, resulting in η equals 91.4 % and Q_{avg} equals 0.207 pu. In contrast, the proposed method (case 2) implements the MOPSO algorithm to optimize K_{fl}, achieving full ZVS while reducing reactive power by 28.9 %. Although this approach slightly reduces the utilization of the power rating, the proposed method achieves a lower value of Euclidean distance $l(x)$ by 14.6 % which demonstrates a more balanced trade-off and improved design.

To balance R and Q_{avg} under a fixed power rating utilization η with a 30 % overload margin, case 3 yield design parameters similar to those of the conventional approach. However, it reduces reactive power by 9.6 % while slightly decreasing the ZVS region. Additionally, the proposed method achieves a 7.2 % lower $l(x)$ value, demonstrating its ability to effectively balance these competing objectives.

To minimize reactive power and current stress, case 4 achieves the lowest reactive power $Q_{\text{avg}} = 0.096$ pu. The methods in [5] and [12] do not account for variations in voltage conversion ratio and load conditions, leading to relatively higher reactive power. The $l(x)$ value, representing the distance from $Q_{\text{avg}} = 0$, confirms a better optimization capability of the proposed method, achieving a value of $l(x)$ of 52.9 % lower than [5] and 38.9 % lower than [12].

For multi-objective optimization, Case 1 demonstrates better overall performance. Thanks to the optimized parameters $N = 2.04$ and $K_{fl} = 9.01$, and the TPS modulation, the DAB converter achieves a well-balanced trade-off, with $R = 95.3\,\%$, $\eta = 79.2\,\%$, and $Q_{\text{avg}} = 0.155$ pu. Although its individual performance in three objectives is moderate, Case 1 achieves the best overall evaluation with $l(x) = 0.753$, ensuring a highly optimized design. In particular, it reduces the reactive power by 24 % compared with [5] and 1.3 % compared with [12], respectively. These results highlight the effectiveness of the proposed method in achieving high ZVS performance, improved utilization, and minimal reactive power, making it a global optimized solution for practical applications.

V. EXPERIMENTAL RESULTS

A. Validation of the Proposed Design Method

The above-mentioned four DAB design scenarios are validated on a 1 kW scale-down prototype, as shown in Fig. 13. The experimental setup follows the droop control curve with

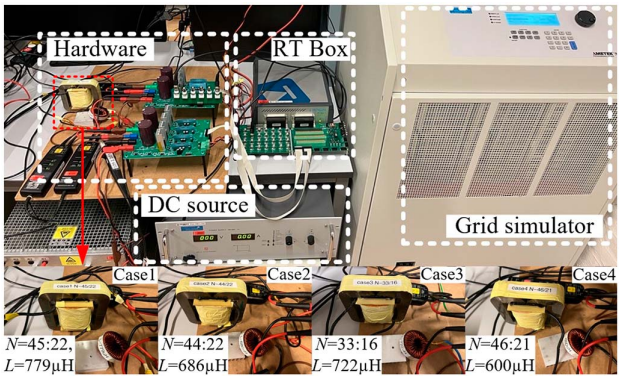

Fig. 13. Experimental setup.

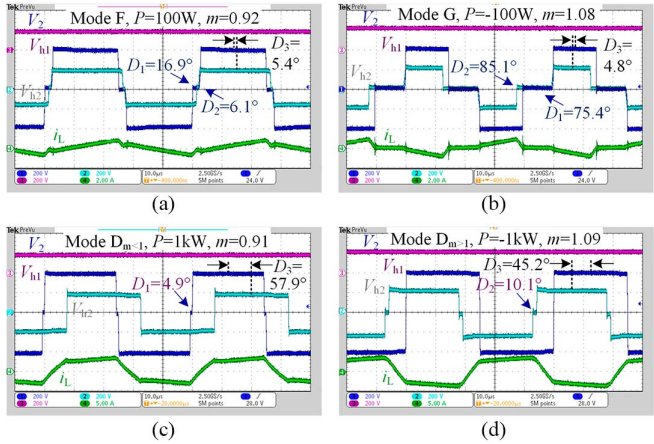

Fig. 14. Experimental waveforms of the DAB converter for case 1. (a) Mode F. (b) Mode G. (c) Mode $D_{m<1}$. (d) Mode $D_{m>1}$.

TABLE IV
SYSTEM CONFIGURATION AND DESIGN PARAMETERS

Primary Voltage V_1	400 V	Secondary Voltage V_{2b}	200 V
Maximum power P_{d_max}	1 kW	Operation range m	[0.91,1.09]
Switching frequency f_s	20 kHz	Power switch	NGTB50N120FL2WG
Case 1 $N = 2.04$, $K_{fl} = 15.57$, $R = 93.6\%$, $\eta = 83.8\%$, $Q_{\text{avg}} = 0.168$ pu			
Case 2 $N = 2$, $K_{fl} = 13.71$, $R = 100\%$, $\eta = 75.3\%$, $Q_{\text{avg}} = 0.162$ pu			
Case 3 $N = 2.06$, $K_{fl} = 14.44$, $R = 92.3\%$, $\eta = 76.9\%$, $Q_{\text{avg}} = 0.144$ pu			
Case 4 $N = 2.19$, $K_{fl} = 12.01$, $R = 71.4\%$, $\eta = 60.3\%$, $Q_{\text{avg}} = 0.095$ pu			

TABLE V
SPECIFICATIONS OF THE TRANSFORMERS AND INDUCTORS

	Transformer	Turns ratio	Inductor	Value
Case 1	Core: FT-3M	$N = 2.04\,(45/22)$	Core: T130-52	$L = 779\,\mu$H
Case 2	Nanocrystal	$N = 2\,(44/22)$	Toroid	$L = 686\,\mu$H
Case 3	Size: 90 × 90	$N = 2.06\,(33/16)$	Wire: AWG 16	$L = 722\,\mu$H
Case 4	×33 mm	$N = 2.19\,(46/21)$		$L = 600\,\mu$H

forward and backward power flow modes. The system configuration and design parameters are summarized in Table IV has four sets of transformers and inductors, corresponding to four cases, are developed. The specifications of the transformers and inductors are listed in Table V. The transformer adopts a P–S–P interleaved winding structure, where the primary winding is split into two 23-turn and halves symmetrically arranged around the 21-turn secondary, as implemented in Case 4. This arrangement enhances magnetic coupling and effectively reduces leakage inductance [24]. Additionally, nanocrystalline core material is employed in this design, offering both low magnetizing inductance and a high quality factor due to its high permeability and low core losses [25].

Fig. 14 presents the waveforms of Case 1 under four operation modes. As shown in Fig. 14(a), under forward power transmission $P = 100$ W and $m = 0.92$, the DAB converter operates in mode F with PS angle $D_1 = 16.9°$, $D_2 = 6.1°$, $D_3 = 5.4°$. The inductor current closes to 0 as the voltage V_{h1} steps to 400 V, satisfying the zero-current-switching (ZCS) operation conditions. Fig. 14(b) demonstrates mode G under backward power transmission at $P = -100$ W and $m = 1.08$, also achieving ZCS. Fig. 14(c) and (d) illustrates the operation mode $D_{m<1}$ with $D_2 = 0$ and mode $D_{m<1}$ with $D_1 = 0$, respectively. In each mode, the polarity of the inductor current ensures the ZVS conditions for all devices.

Fig. 15(a1)–(c1) presents the waveforms of cases 2–4 under forward power transmission conditions ($P = 1$ kW, $m = 0.91$). It can be seen that the polarity of the inductor current in each case satisfies the ZVS conditions, aligned with the mode D operation ($m < 1$) with $D_2 = 0$. Although all four cases meet ZVS conditions, their optimization objectives lead to distinct performance characteristics. For example, case 1 exhibits the highest peak value of the inductor current ($i_{peak} = 4.1$ A), while case 4 achieves the smallest PS ($D_3 = 36.8°$) to minimize reactive power. Fig. 15(a2)–(d2) illustrates the waveforms under backward power transmission conditions ($P = -1$ kW, $m = 1.09$). The power switches can achieve ZVS TURN-ON, corresponding to mode D operation D ($m > 1$) with $D_1 = 0$. Case 2 and case 3 emphasis on full ZVS operation and fixed utilization, respectively. However, their optimization results yield similar utilization levels, leading to comparable PS angles when the DAB converter transmit the maximum power. The outer and inner PS angles are $D_2 = 9.2°$, $D_3 = 39.2°$ for case 2 and $D_2 = 12.1°$, $D_3 = 40.6°$ for case 3, respectively.

Fig. 16 compares the experimental and theoretical phase shift angles and reactive power across ten test points for the four cases. Case 4 achieves the smallest phase shift angle $-30.9°$ to $36.8°$ and the lowest average reactive power $Q_{\text{avg}} = 0.095$ pu. However, as shown in Table IV, it has the lowest utilization $\eta = 60.3\,\%$. Case 2 prioritizes the full ZVS operation while optimizing utilization and reactive power, leading to the utilization and reactive power levels $\eta = 75.3\,\%$ and $Q_{\text{avg}} = 0.162$ pu comparable to Case 3 $\eta = 76.9\,\%$ and $Q_{\text{avg}} = 0.144$ pu. From the global optimization perspective, case 1 achieves the best trade-off, offering the highest utilization $\eta = 83.8\,\%$ while moderate ZVS range and reactive power, $R = 93.6\,\%$ and $Q_{\text{avg}} = 0.168$ pu. The maximum deviation between the theoretical and experimental PS angle D_3 reaches 3.9° at $m = 0.91$ in case 1. These deviations could be attributed to circuit nonidealities and additional losses. For example, as the transferred power

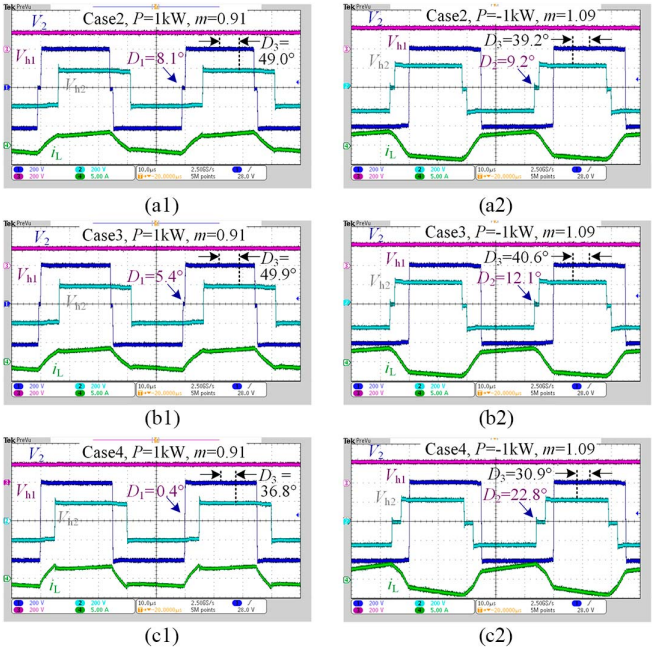

Fig. 15. Experimental waveforms of the DAB converter with cases 2–4. (a1)–(c1) Forward power flow $P = 1$ kW, $m = 0.91$. (a2)–(c2) Backward power flow $P = -1$ kW, $m = 1.09$.

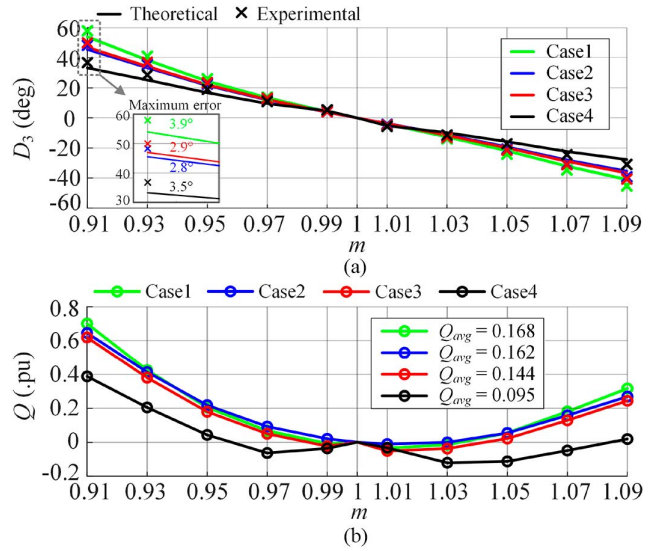

Fig. 16. Experimental curves of the phase shift angle and reactive power for four cases. (a) The theoretical and experimental phase shift angle D_3. (b) Reactive power of four cases.

rises, increased switching and copper losses leads to extra phase lag compared with theoretical results. Furthermore, dead time effects and output capacitance nonlinearity in the IGBTs affect the actual commutation interval, resulting in the angle error [26], [27].

Fig. 17 presents the experimental efficiency results for the four cases. It can be observed that Case 4 achieves the highest efficiency $\eta = 95.9\,\%$ under full load conditions. In contrast, case 1 yields slightly lower efficiency $\eta = 93.4\,\%$ at high loads,

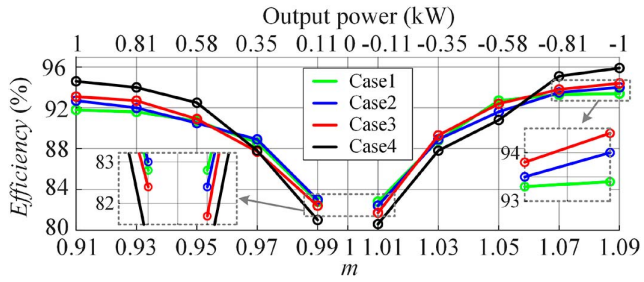

Fig. 17. Experimental efficiency of the DAB converter under four cases.

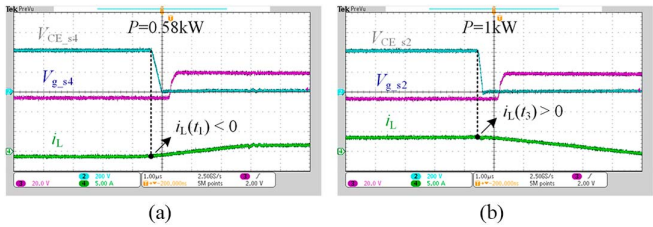

Fig. 18. ZVS Achievement details in HB1. (a) Switch S_4. (b) switch S_2.

while delivering the best overall balance ($R = 93.6\,\%$, $\eta = 83.8\,\%$, $Q_{\text{avg}} = 0.168$ pu). This reflects the inherent trade-off in our multi-dimensional framework: case 1 sacrifices 2.5 % of efficiency to gain over 22 % in ZVS range and 23.5 % in power-rating utilization. The efficiency of case 2 and case 3 falls between other cases, aligning with the previous reactive power results and analysis. These findings validate the effectiveness of the proposed design guideline.

B. ZVS and Dynamic Performance

Fig. 18 shows the ZVS TURN-ON process for two switches (S_2 and S_4) in the high-voltage side of case 1. In Fig. 18(a), at $t = t_1$, the polarity of the inductor current is negative, and the collector emitter voltage V_{CE_s4} of switch S_4 starts to decrease due to resonant commutation. Once the voltage drops to zero, the gate-emitter voltage V_{g_s4} turns positive and turns ON switch S_4, thereby achieving the ZVS operation. A similar sequence is observed in Fig. 18(b) for switch S_2, where V_{CE_s2} drops to zero before V_{g_s2} rises, confirming successful ZVS.

In this case, the dynamic response test is conducted, where the power transmission condition increases from $P = 0.58$ kW to $P = 1$ kW. As shown in Fig. 19, it can be seen that the phase shift angle D_3 changed from 25.9° to 57.9° confirms the increase in power transfer, while the converter reaches the target power and stabilizes within 600 μs. The inductor current waveform shows negligible overshoot or undershoot during this transition. These results demonstrate that the optimized parameters N and K_{fl} ensure both optimized steady-state operation and robust dynamic response under load variations.

Fig. 20 illustrates the experimental waveforms for case 1 under light load conditions. In Fig. 20(a), the DAB converter operates in mode F to transmit 50 W at $m = 0.95$. Fig. 19(b) shows the TURN-ON transition of S_4. At $t = t_1$, the inductor current approaches to zero, while V_{CE_4} starts to drop. After

TABLE VI
COMPARATIVE ASSESSMENT OF DAB CONVERTER DESIGNS

Ref	Design Variables	Optimization Objectives	Modulation	Prototype Voltage	ZVS Range	Utilization	Reactive Power	Efficiency	Power Density
[5]	K_{fl}	Improve ZVS range	SPS	700 V / 350 V	100 %	26.5 %	0.208 pu	++	+
[12]	N, L	Optimize current stress	TPS	40 V / 40 V	89.1 %	59.5 %	0.170 pu	+++	+
Proposed (case4)	N, K_{fl}	Minimize reactive power	TPS	400 V / 200 V	71.4 %	60.3 %	0.095 pu	+++	++

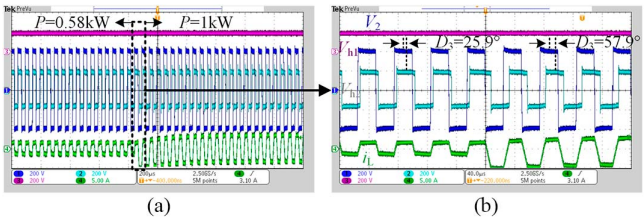

Fig. 19. Dynamic response experiment for case 1. (a) Overall transition. (b) Zoomed in view of the transition.

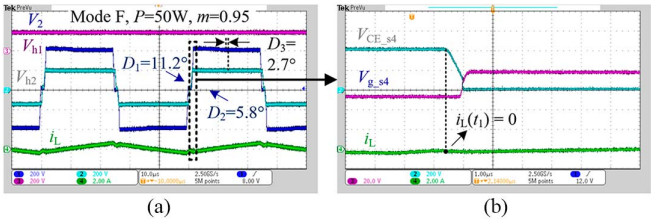

Fig. 20. Experimental waveforms under light load conditions. (a) Operation conditions. (b) ZCS achievement in switch S_4.

650 ns, the gate emitter voltage V_{g_s4} increases while the inductor current remains at $i_L = 0$ A, confirming S_4 achieves ZCS TURN-ON under light load conditions. These experiment results across different load conditions demonstrate that the proposed design achieves soft switching.

C. Comparison With Design Methods [5], [12]

The proposed design method (case 4) is compared with the presented method [5], [12]. The transformer turns ratio and series inductance designed by the method [5], [12] are $N = 2$, $L = 240\,\mu$H and $N = 1.94$, $L = 520\,\mu$H, respectively. Fig. 21 compares the reactive power for proposed method and existing methods. It can be seen that the reactive power curve of the proposed method (case 4) is closer to curve $Q = 0$ compared with the design methods [5], [12], and it achieves the lowest average reactive power ($Q_{\text{avg}} = 0.095$ pu). By lowering reactive power, the converter's apparent power gets reduced, which directly decreases transformer's rms current as given by (27). Furthermore, this reduction in power losses $I_{\text{rms}}^2 R_{\text{loss}}$ contributes to improved efficiency and reduced thermal stress

$$S = V_{h1\text{rms}} I_{\text{rms}} = \sqrt{\sum_{n=1,3,5,\ldots} P_n^2 + \sum_{n=1,3,5,\ldots} Q_n^2 + \sum_{m\neq n=1,3,5,\ldots} Q_{m\neq n}^2}. \tag{27}$$

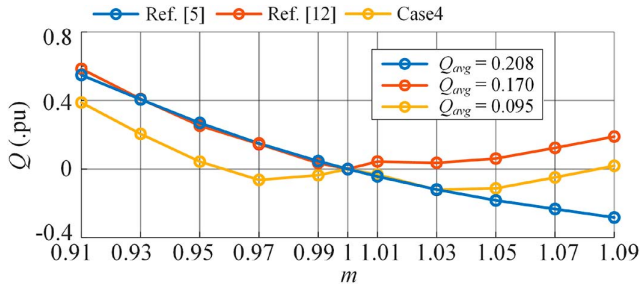

Fig. 21. Reactive power comparison of proposed method (case 4) and other methods.

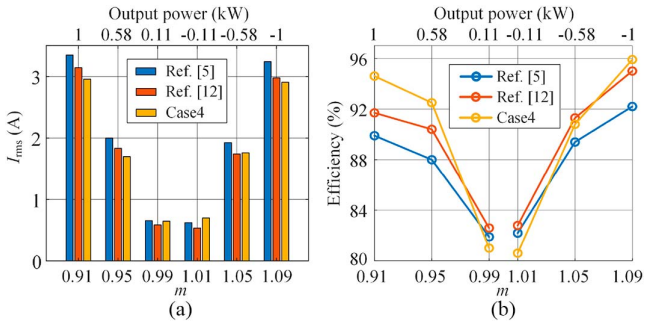

Fig. 22. Experimental results comparison on: (a) the rms current; and (b) the efficiency.

Fig. 22 presents the rms current and efficiency experiment comparison. As shown in Fig. 22(a), the rms current of case 4 performs the lowest rms current ($I_{\text{rms}} = 2.99$ A, $I_{\text{rms}} = 2.90$ A) at $m = 0.91$ and $m = 1.09$, which is consist with its minimized reactive power in Fig. 21. The efficiency of case 4 in Fig. 22(b) archives the highest efficiency under 100 % load condition compared with methods [5], [12]. The rms current and efficiency results demonstrate the effectiveness of the proposed design method in minimizing the reactive power while enhancing efficiency.

Table VI provides a comparative assessment of different DAB converter designs. The method in [5] optimizes series inductances to extend ZVS range, achieving 100 % ZVS operation. However, it brings additional costs in utilization and reactive power. In contrast, [12] optimizes the transformer turns ratio N and inductance L using TPS modulation, improving system utilization and efficiency. However, this method provides only a limited benefit in reducing reactive power (18.2 %).

The proposed design (Case4) prioritizes reactive power minimization through optimization of N and K_{fl}, reducing reactive power to 0.095 pu and further enhancing efficiency. By lowering reactive power, the converter's apparent power requirement is reduced, enabling smaller magnetic components and thus higher power density.

VI. Conclusion

The dc grid-forming DAB converter is the key element in future LVdc systems. This article characterizes DAB converters across three critical design dimensions: ZVS operation, power rating utilization, and reactive power optimization. An analytical framework and a multidimensional design method based on MOPSO are proposed to optimize the transformer turns ratio N and inductance-switching frequency product K_{fl}. Its adoption not only signifies achieving a global and well-balanced DAB design goals but also delivers tailored benefits from techno-economic for operators to meet specific DAB requirements. The benefits are analyzed and tested to achieve complete ZVS operation (case 2), ensure power rating under fixed conditions (case 3), and minimize reactive power (case 4). Theoretical analysis and experimental results are well matched, which confirms the effectiveness of the proposed DAB design method in LVdc applications.

Furthermore, this design framework could be extended to medium-voltage, high-voltage and high-power applications, as the core relationships among ZVS capability, converter utilization, and reactive power remain valid at any voltage and power level. It can be further enhanced by integrating advanced control strategies, modular converter topologies, and expanded multi-objective optimization models that capture both electrical performance objectives and practical implementation constraints.

References

[1] S. Shao et al., "Modeling and advanced control of dual-active-bridge dc-dc converters: A review," *IEEE Trans. Power Electron.*, vol. 37, no. 2, pp. 1524–1547, Feb. 2022.

[2] X. Zhu et al., "Optimal control strategy with efficiency and reliability improvement for offshore dc microgrids," *IEEE Trans. Power Electron.*, vol. 40, no. 11, pp. 16728–16739, Nov. 2025.

[3] I. Khan, S. Rahman, M. A. Ayaz, M. Amir, and H. Shehada, "Review of isolated dc-dc converters for application in data center power delivery," *IEEE Trans. Ind. Appl.*, vol. 60, no. 4, pp. 5436–5446, Jul./Aug. 2024.

[4] N. Hou, P. Gunawardena, X. Wu, L. Ding, Y. Zhang, and Y. W. Li, "An input-oriented power sharing control scheme with fast-dynamic response for ISOP DAB dc-dc converter," *IEEE Trans. Power Electron.*, vol. 37, no. 6, pp. 6501–6510, Jun. 2022.

[5] E. L. Carvalho, A. Sidorova, A. Blinov, A. Chub, and D. Vinnikov, "Design considerations of dual-active bridge dc grid-forming converter for dc buildings," *IEEE Trans. Ind. Electron.*, vol. 71, no. 9, pp. 10601–10611, Sep. 2024.

[6] N. Hou and Y. W. Li, "Overview and comparison of modulation and control strategies for a nonresonant single-phase dual-active-bridge dc-dc converter," *IEEE Trans. Power Electron.*, vol. 35, no. 3, pp. 3148–3172, Mar. 2020.

[7] Z. Guo, Z. Chen, and Z. Chen, "Pareto optimum design of the magnetic components in DAB converters based on nondominated sorting genetic algorithms-II," *IEEE Trans. Power Electron.*, vol. 38, no. 10, pp. 12961–12974, Oct. 2023.

[8] B. Zhao, Q. Song, W. Liu, G. Liu, and Y. Zhao, "Universal high-frequency-link characterization and practical fundamental-optimal strategy for dual-active-bridge dc-dc converter under PWM plus phase-shift control," *IEEE Trans. Power Electron.*, vol. 30, no. 12, pp. 6488–6494, Dec. 2015.

[9] A. Rodriguez, A. Vazquez, D. G. Lamar, M. M. Hernando, and J. Sebastian, "Different purpose design strategies and techniques to improve the performance of a dual active bridge with phase-shift control," *IEEE Trans. Power Electron.*, vol. 30, no. 2, pp. 790–804, Feb. 2014.

[10] D. Das and K. Basu, "Optimal design of a dual-active-bridge dc-dc converter," *IEEE Trans. Ind. Electron.*, vol. 68, no. 12, pp. 12034–12045, Dec. 2021.

[11] A. Sengupta, T. Pereira, and M. Liserre, "Design optimization of dual active bridge converter for supercapacitor application," *IEEE Trans. Power Electron.*, vol. 39, no. 9, pp. 11544–11557, Sep. 2024.

[12] H. Zhang, Z. Liu, Y. Song, P. Han, and J. Liu, "A current-stress-optimized design method for dual active bridge converters with improved ZVS capability under wide output voltage conditions," *IEEE Trans. Ind. Electron.*, vol. 71, no. 6, pp. 5807–5817, Jun. 2024.

[13] X. Yang, J. Wang, Y. Du, C. Liu, T. Zhang, and J. Zhang, "Bidirectional ZVS operation of all switches for a DAB converter over a full range of loads with optimized current stress," *IEEE Trans. Ind. Appl.*, vol. 60, no. 1, pp. 1183–1195, Jun. 2024.

[14] D. Mou, Q. Luo, J. Li, Y. Wei, and P. Sun, "Five-degree-of-freedom modulation scheme for dual active bridge dc-dc converter," *IEEE Trans. Power Electron.*, vol. 36, no. 9, pp. 10584–10601, Sep. 2021.

[15] X. Li, X. Zhang, F. Lin, C. Sun, and K. Mao, "Artificial-intelligence-based triple phase shift modulation for dual active bridge converter with minimized current stress," *IEEE J. Emerg. Sel. Top. Power Electron.*, vol. 11, no. 4, pp. 4430–4441, Aug. 2023.

[16] Y. Tang et al., "Deep reinforcement learning aided variable-frequency triple-phase-shift control for dual-active-bridge converter," *IEEE Trans. Ind. Electron.*, vol. 70, no. 10, pp. 10506–10515, Oct. 2023.

[17] E. L. Carvalho, C. A. Felipe, L. V. Bellinaso, C. M. de Oliveira Stein, R. Cardoso, and L. Michels, "Asymmetrical-PWM DAB converter with extended ZVS/ZCS range and reduced circulating current for ESS applications," *IEEE Trans. Power Electron.*, vol. 36, no. 11, pp. 12990–13001, Nov. 2021.

[18] Q. Gu, L. Yuan, J. Nie, J. Sun, and Z. Zhao, "Current stress minimization of dual-active-bridge dc–dc converter within the whole operating range," *IEEE J. Emerg. Sel. Top. Power Electron.*, vol. 7, no. 1, pp. 129–142, Mar. 2019.

[19] M. Reyes-Sierra et al., "Multi-objective particle swarm optimizers: A survey of the state-of-the-art," *Int. J. Comput. Intell. Res*, vol. 2, no. 3, pp. 287–308, 2006.

[20] B. Zhao and X. Zhang, "An efficiency-oriented two-stage optimal design methodology of high-frequency LCLC resonant converters for space travelling-wave tube amplifier applications," *IEEE Trans. Ind. Electron.*, vol. 67, no. 2, pp. 1068–1080, Feb. 2020.

[21] S. Verma, M. Pant, and V. Snasel, "A comprehensive review on NSGA-II for multi-objective combinatorial optimization problems," *IEEE Access*, vol. 9, pp. 57757–57791, 2021.

[22] C. A. C. Coello, G. T. Pulido, and M. S. Lechuga, "Handling multiple objectives with particle swarm optimization," *IEEE Trans. Evol. Comput.*, vol. 8, no. 3, pp. 256–279, Jun. 2004.

[23] Y. Cui, X. Meng, and J. Qiao, "A multi-objective particle swarm optimization algorithm based on two-archive mechanism," *Appl. soft Comput.*, vol. 119, 2022, Art. no. 108532.

[24] Z. Ouyang, O. C. Thomsen, and M. A. E. Andersen, "The analysis and comparison of leakage inductance in different winding arrangements for planar transformer," in *Proc. Int. Conf. Power Electron. Drive Syst. (PEDS)*, 2009, pp. 1143–1148.

[25] S. Balci, I. Sefa, and N. Altin, "Design and analysis of a 35 kva medium frequency power transformer with the nanocrystalline core material," *Int. J. Hydrogen Energy*, vol. 42, no. 28, pp. 17895–17909, 2017.

[26] Y. Xu, C. N. M. Ho, A. Ghosh, and D. Muthumuni, "An electrical transient model of IGBT-diode switching cell for power semiconductor loss estimation in electromagnetic transient simulation," *IEEE Trans. Power Electron.*, vol. 35, no. 3, pp. 2979–2989, Mar. 2020.

[27] X. Wei, B. Yao, Y. Peng, Y. Sun, K. Wang, and H. Wang, "An improved discharge profile-based dc-link capacitance estimation for traction inverter in electric vehicle applications," *IEEE Trans. Power Electron.*, vol. 39, no. 7, pp. 8696–8708, Jul. 2024.